Numerical simulation and comparison with experiments of a floating wind turbine using a direct forcing method

P.A. Berthelsen & M. Thys
SINTEF Ocean, Trondheim, Norway

A. Kamath, T. Martin & H. Bihs
Department of Civil and Environmental Engineering, Norwegian University of Science and Technology, Trondheim, Norway

ABSTRACT: The open-source Computational Fluid Dynamic (CFD) code REEF3D is used to simulate the hydrodynamic loads and motion response of a floating wind turbine substructure, the INO WINDMOOR semi-submersible floating wind turbine. REEF3D uses the level set method to model the free surface and the direct forcing method is applied to calculate the hydrodynamic coupling between the fluid and the rigid body of the floater, including six degrees-of-freedom (6DOF) motion response. The numerical simulations are compared with experimental data from the WINDMOOR project for validation of the results, and this includes decay tests in surge, heave and pitch as well as the 6DOF motion of the moored substructure exposed to regular waves. Results show acceptable agreement between experimental and numerical data.

1 INTRODUCTION

Accurate and validated numerical simulation methods are an essential part of designing cost-effective and reliable offshore structures. For moored floating structures it is important to have accurate wave load calculations in order to predict correct low frequency responses in extreme waves. This is important for the design of mooring systems since the low frequency horizontal motions at resonance are very sensitive to the excitation level and the damping level due to dynamic amplification. Computational Fluid Dynamics (CFD) methods, albeit computational demanding, are expected to become more relevant as a tool for designing new substructures. However, CFD results can be highly sensitive to choices of numerical methods, implementation and user input. Thorough validation of numerical results using measured data is needed to develop sufficient confidence in the applicability of these tools and establish a standard procedure for implementation, setup and execution to aid in cost-effective and reliable design.

The main advantage of using the Navier-Stokes (NS) equations for the simulation of floating structures is the ability to resolve most of the fluid physics with few assumptions. This makes it possible to investigate nonlinear and resonant phenomena for the innovative designs for further development of floating offshore wind. The major issues to be addressed to employ NS-based solvers for the simulation of floating bodies in waves are: the representation of the free surface, the representation of the complex floating object and the interaction of the fluid with the object. Several methods for the numerical treatment of these aspects are available. The free surface can be represented using either a volume-of-fluids approach (Hirt and Nichols 1981) or the level set method (Osher and Sethian 1988). The representation of the object in the fluid domain can either be carried out using a Lagrangian approach which requires re-meshing of the domain every time the object moves (Ramaswamy et al. 1986), an overset mesh where the object is exists on a secondary mesh that overlaps a base (fluid) mesh and follows the motion of the body (Carrica et al. 2007) or level set representation (Bihs and Kamath 2017). The interaction between the fluid and the object can be represented using an immersed boundary approach with different implementation of boundary conditions such as source term in the momentum equations (Fadlun et al. 2000), or a direct forcing approach where the fluid forces are directly evaluated using Lagrangian markers on the floating body (Uhlmann 2005). The different choices and implementation of the methods results in advantages and limitations of the numerical model.

The current study uses the CFD module in the open-source hydrodynamics solver REEF3D (Bihs

et al. 2016) to simulate the hydrodynamics of a floating offshore wind substructure concept- INO WINDMOOR. The fluid- 6DOF floating body interaction is calculated in a numerical wave tank using the level set method to represent the free surface and the boundary of the body. The direct forcing immersed boundary method is used to evaluate the two-way coupled fluid interaction with the floating body. A quasi-static mooring model is implemented as shown by Martin et al. (2021). The application of such an approach is demonstrated for open-ocean aquaculture structures (Martin et al. 2021). The application of this approach to the modelling of floating offshore wind turbine substructures is presented in the current paper. The study simulates decay tests on the semi-submersible WINDMOOR platform, along with interaction with regular waves. The numerical results for the rigid body motions are compared with the measured data.

2 NUMERICAL MODEL

The numerical analysis is performed using the CFD code REEF3D (Bihs et al. 2016). This open source tool is based on a Cartesian grid framework for modelling of incompressible flow including the immersed boundary method (IBM) for modelling of complex boundaries (interfaces) between two different fluids (two-phase flow) or between a fluid and a structure.

2.1 *Governing Equations*

The flow dynamics can be described by the incompressible Navier-Stokes equations,

$$\nabla \cdot \mathbf{u} = 0, \tag{1}$$

$$\frac{\partial \mathbf{u}}{\partial t} + \mathbf{u} \cdot \nabla \mathbf{u} = -\frac{1}{\rho}\nabla p + \frac{1}{\rho}\nabla \cdot \left\{\mu \left(\nabla \mathbf{u} + \nabla \mathbf{u}^T\right)\right\} + \mathbf{g}, \tag{2}$$

where $\mathbf{u}$ is the flow velocity, ρ is the fluid density, p is the pressure, μ is the viscosity, and $\mathbf{g}$ is the acceleration of gravity.

The free surface is modelled using the level set method (Osher and Sethian 1988, Sussman et al. 1994) where the interface is represented by the zero level set of a signed distance function ϕ. The interface is convected in the flow using the linear advection function

$$\frac{\partial \phi}{\partial t} + \mathbf{u} \cdot \nabla \phi = 0. \tag{3}$$

The fluid properties are smoothed across the interface following the relations

$$\rho(\phi) = \rho_1 + (\rho_2 - \rho_1) H_\epsilon(\phi), \tag{4}$$

$$\mu(\phi) = \mu_1 + (\mu_2 - \mu_1) H_\epsilon(\phi) \tag{5}$$

where ρ_1, ρ_2, and μ_1, μ_2 are the constant densities and viscosities for air (fluid 1) and water (fluid 2), respectively. The smoothed Heaviside function $H_\epsilon(\phi)$ is defined by

$$H_\epsilon(\phi) = \begin{cases} 0, & \text{for } \phi \leq -\epsilon, \\ \frac{1}{2}\left(1 + \frac{\phi}{\epsilon} + \frac{1}{\pi}\sin\left(\frac{\pi\phi}{\epsilon}\right)\right), & \text{for } -\epsilon < \phi < \epsilon, \\ 1, & \text{for } \phi \geq \epsilon \end{cases} \tag{6}$$

where ϵ is a numerical parameter defining the interface thickness. In the present work, ϵ is chosen to be $1.6h$ where h is a characteristic grid cell size.

2.2 *Numerical Solver*

The numerical scheme for solving Eq. (1)-(2) is based on the incremental pressure-correction algorithm (Timmermans et al. 1996). The governing equations (1)-(3) are stepped forward in time using a third-order total variation diminishing (TVD) Runge-Kutta Scheme.

The spatial derivatives are approximated using a finite difference discretisation on a staggered Cartesian grid. The fifth order WENO scheme (Jiang and Shu 1996) is used for the convective terms of Eq. (2) and Hamilton-Jacobi version (Jiang and Peng 2000) is used for Eq. (3). All other terms are discretised with central schemes. The Poisson Equation for pressure is solved iteratively with a geometric fully multi-grid preconditioned (Ashby and Falgout 1996) BiCGStab solver (van der Vorst 1992).

2.3 *Wave Generation and Absorption*

Waves are generated by applying the relaxation method (Mayer et al. 1998, Jacobsen et al. 2012). This means that the free surface and fluid velocities are ramped up to analytical values obtained from wave theory in a zone close to the wave inlet boundary (relaxation zone) following the relation

$$f(\tilde{\chi})_{relaxed} = \Phi(\tilde{\chi}) f_{analytical} + (1 - \Phi(\tilde{\chi})) f_{computed}, \tag{7}$$

where f represent the velocity vector $\mathbf{u}$ or the level set function ϕ, $\tilde{\chi}$ is spatial coordinate scaled to the length of the relaxation zone, and Φ is the relaxation function defined as

$$\Phi(\tilde{\chi}) = 1 - \frac{e^{\tilde{\chi}^{3.5}} - 1}{e - 1} \quad \text{for } \tilde{\chi} \in [0; 1]. \tag{8}$$

The relaxation method is also used to dampen or absorb outgoing waves near the outlet boundaries in order to suppress numerical reflection of the waves.

2.4 *Solid Boundary*

The boundary conditions at the solid interface between the floater and the ambient flow are handled through a direct forcing immersed boundary method (Martin et al. 2021, Yang 2018). This involves adding a forcing term to the intermediate velocity field $\mathbf{u}^*$ before solving for pressure. This forcing term is defined as

$$\mathbf{f}^* = H_\epsilon(\phi_s^*)\left(\frac{P(\mathbf{u}^*) - \mathbf{u}^*}{\alpha_k \Delta t}\right), \tag{9}$$

where $H_\epsilon(\phi_s^*)$ is the smoothed Heaviside function given by Eq. (6), ϕ_s^* is a level set function describing the fluid-solid boundary of the floating object. $P(\mathbf{u}^*)$ represent the projection of the intermediate velocity field

$$P(\mathbf{u}^*) = \dot{\mathbf{x}}_s + \omega_s \times \mathbf{r}, \tag{10}$$

where $\dot{\mathbf{x}}_s$ and $\omega_s \times \mathbf{r}$ are the translational and rotational rigid body velocities given in the inertial frame of reference, and $\mathbf{r}$ is the distance vector going from the rigid body's origin (centre of gravity) to the position where $P(\mathbf{u}^*)$ is computed.

The fluid forces and momenta acting on the floating body are calculated by integrating the pressure p and the viscous stress tensor τ over the solid surface Γ of the structure,

$$\mathbf{F} = \int_\Gamma (-p\mathbf{n} + \tau\mathbf{n})\, \mathrm{d}\Gamma, \tag{11}$$

$$\mathbf{M} = \int_\Gamma \mathbf{r} \times (-p\mathbf{n} + \tau\mathbf{n})\, \mathrm{d}\Gamma, \tag{12}$$

where $\mathbf{n}$ is the unit normal vector on the body surface pointing outwards, and $\mathbf{r}$ is the distance vector pointing from the body's origin to the surface.

3 CASE STUDY

The INO WINDMOOR semisubmersible floating wind turbine (Souza et al. 2021) is used as case study in this work. This triangular shaped floating platform consist of three columns connected by pontoons and deck beams, with a wind turbine tower extending from one of the columns. In the present study, only the semisubmersible platform is included in the simulation, i.e. aerodynamic loads on the tower and rotor blades are ignored. The shape of the substructure is illustrated in Fig. 1 and the main dimensions of the prototype are summarised in Tab. 1.

Numerical simulations are compared with results from the WINDMOOR experiments performed at SINTEF's Ocean Basin in 2020 (Thys et al. 2021). Decay tests in surge, heave and pitch and tests with regular waves are used as benchmark cases for validation of the CFD results.

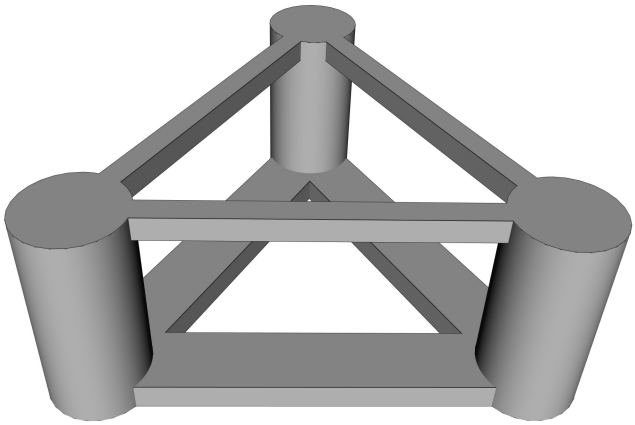

Figure 1: The INO WINDMOOR semisubmersible platform

Table 1: Main dimensions of the INO WINDMOOR platform.

Parameter	Unit	Value
Column diameter	m	15.0
Column height	m	31.0
Pontoon width	m	10.0
Pontoon height	m	4.0
Column centre-centre distance	m	61.0
Deck-Beam width	m	3.5
Deck-Beam height	m	3.5
Draft	m	15.5

3.1 *Experimental Data*

The model experiments were carried out at a 1:40 Froude scale, where the floater and tower were modelled as rigid bodies with a spring element connecting the two parts to match the towers 1st elastic mode. A simplified horizontal mooring system was used for the experiments. This model scale mooring system was designed to reproduce the linearised horizontal stiff-

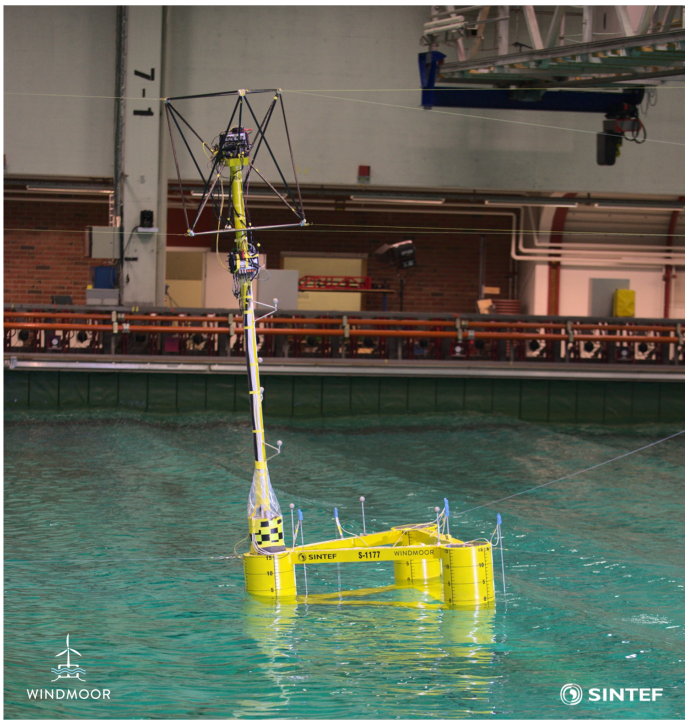

Figure 2: The 1/40 scale model of the INO WINDMOOR floating wind turbine in SINTEF Ocean's test facility.

Table 2: Mass properties for the INO WINDMOOR floating wind turbine (data in full scale) as used in simulations. The radius of gyrations (r_{xx}, r_{yy} and r_{zz}) are all given with respect to COG, where COG is relative to still water level and the (horizontal) geometric centre of the model, positive $z-$direction is upwards.

Parameter	Unit	Value
Mass	t	14124.0
r_{xx}	m	43.62
r_{yy}	m	44.01
r_{zz}	m	29.87
COG_x	m	0.00
COG_y	m	0.00
COG_z	m	3.94

ness of the prototype semi-taut catenary system. The mooring system was made of three wire-chain-spring lines, connected to fairleads at the top of the columns and anchor points positioned around the basin. All the lines were above-water to avoid any hydrodynamic loads on the lines and to remove uncertainty related to mooring damping.

Figure 2 shows the model of the floating wind turbine in the Ocean Basin. The tank measures 80 m by 50 m. The water depth during the tests was 3.75 m (150 m in full scale). Aerodynamic loads on the turbine and tower were simulated externally in real-time and imposed on the model through an actuator system connected with wires to a frame on top of the tower using the Real-Time Hybrid Model (ReaTHM®) testing method (Sauder et al. 2016, Thys et al. 2021). Only tests without wind loads has been used for comparison with numerical simulations in the present work.

The position of the model was measured with an optical-electronic system consisting of land-based cameras and reflective diodes mounted on the floating model. Translational accelerations were also measured with accelerometers, and mooring line tensions with a Z-transducer. Wave elevations was measured at three different locations in the basin with conductance-type wave probes, and relative wave elevation was measured at six locations around the model.

The mass properties of the floating wind turbine are given in Tab. 2 based on as-built data (Thys et al. 2021). The location of the centre of gravity (COG) is given with respect to the geometric centre of the floater at the still water level.

3.2 *Numerical Setup*

The numerical analysis are carried out at model scale (1:40), but the results presented are scaled up to prototype scale. Each line from the horizontal mooring system is replaced by a simpler linear spring equation:

$$F = F_0 + k \cdot \delta l, \tag{13}$$

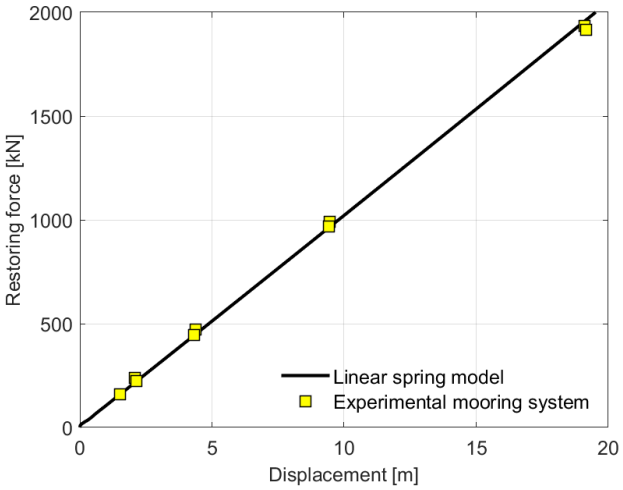

Figure 3: The mooring restoring force-displacement curve.

where F_0 is the spring pretension (at still water equilibrium position), k is an equivalent linear spring stiffness, and δl is the extension of the spring. The equivalent spring stiffness coefficient k was chosen to reproduce the experimental mooring force–displacement curve for horizontal offsets (see Fig. 3).

To reduce the computational effort, a smaller domain than the actual tank size was used in the numerical

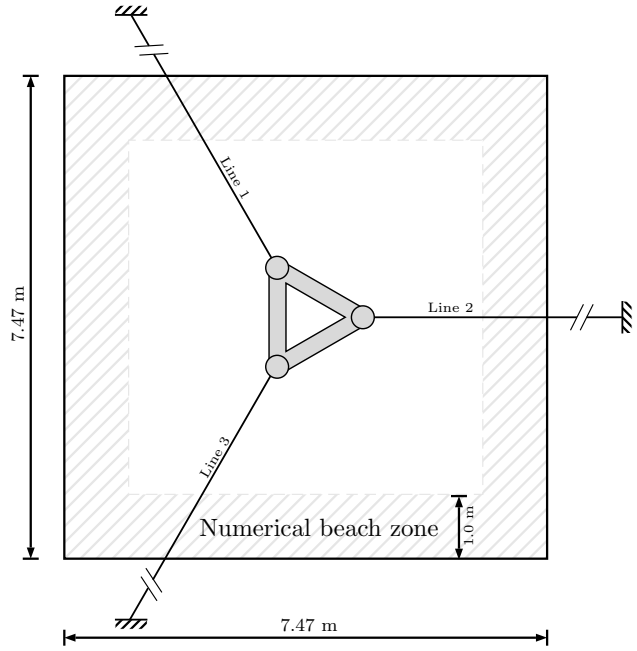

(a) Decay tests.

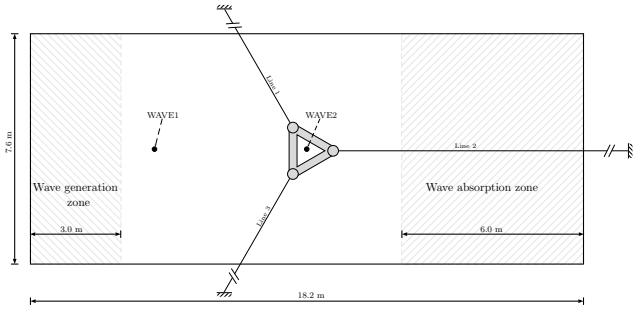

(b) Regular wave tests.

Figure 4: Setup for numerical analysis.

Table 3: Grid properties for decay tests (numbers in model scale).

Grid	$\Delta x_{\min}$ $\Delta y_{\min}$ $\Delta z_{\min}$ [m]	$\Delta x_{\max}$ $\Delta y_{\max}$ [m]	Number of grid cells Decay [-]	Regular waves [-]
Coarse	0.020	0.10	2,464,900	4,213,500
Medium	0.010	0.08	6,994,800	10,533,600
Fine	0.007	0.07	12,493,200	18,227,200

simulation. For the decay tests, the numerical tank measures (in model scale) 7.47 m $\times$ 7.47 m and the height of the computational domain is 5 m (with the free surface located 3.75 m above the bottom). Wall boundaries are used at the exterior boundaries and a numerical beach is applied near the walls with a relaxation zone of 1.0 m length. The initial position of the floater is in the centre of the tank. Figure 4a shows the numerical setup of the decay tests.

A rectangular shaped numerical tank 18.2 m long and 7.6 m wide (in model scale) is used for simulations with regular waves. The height of the domain is 5 m and the water depth is 3.75 m. Wall boundaries are used on the long side walls, a 3.0 m wave relaxation zone is applied at the inlet boundary and a 6.0 m wide wave absorption zone is applied at the outlet. The floater is positioned 9.078 m downstream of the wave inlet. Figure 4 shows the numerical setup. In addition, two numerical wave gauges are placed in the numerical tank with same position relative to the floater as in the experiment.

Three different grid resolution were applied in the decay simulations for evaluation of the grid sensitivity. The grid cell size is constant in the horizontal direction in a square region surrounding the floater (for 3.0 m $\leq x \leq$ 4.8 m and 2.8 m $\leq y \leq$ 4.6 m). A linear grid stretching algorithm is applied in the horizontal direction away from this high resolution region where a stretching factor of 1.3 is used with an upper limit on the cell size. The grid cells are stretched in the vertical direction using a $\sinh$-function with stretching factor 2.5 and focus point located at the still water level (3.75 m above bottom boundary). See Fig. 5 for illustration of the grid near the floating platform.

The grid used for the simulations with regular wave is similar to the ones used for decay tests with the high resolution region adapted to the shifted position of the platform. The cell size in $x-$direction is constant for 8.1 m $\leq x \leq$ 9.9 m and in $y-$direction for 2.9 m $\leq y \leq$ 4.7 m. The grid cells are stretched with a factor of 1.3 in the horizontal direction outside this region up to a maximum cell size to ensure good wave generation and propagation in the region towards the floating platform. The vertical discretisation is identical to the model for the decay simulations. Table 3 summarise the grid setup and cell sizes for the different grid resolutions. The simulation time step, Δt, is adaptive and selected to satisfy CFL=0.1 (Courant–Friedrichs–Lewy condition) throughout the simulations.

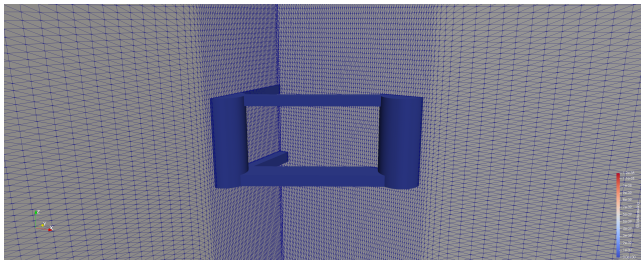

Figure 5: Screenshot of the coarse mesh showing the high resolution region near the platform.

Table 4: Natural periods from experiment and numerical simulations.

Mode	Experiment [s]	Grid resolution Fine [s]	Medium [s]	Coarse [s]
Surge	93.8	97.2	99.6	104.3
Heave	16.6	18.0	18.4	19.1
Pitch	30.4	29.8	30.0	30.3

4 RESULTS AND DISCUSSIONS

4.1 *Numerical decay tests*

Numerical decay tests are performed in surge, heave and pitch, and compared with experimental decay tests. The natural periods are governed by the platform inertia (structural mass and added mass) and stiffness properties. Platform inertia and mooring stiffness are given as measured values from the experiments; thus, the accuracy of calculated natural periods will be determined by the CFD-codes ability to accurately calculate added mass and hydrostatic stiffness. The decay simulations were initiated by releasing the platform from a position slightly offset from its static equilibrium position in calm water. The offset applied in surge, heave and pitch were 11 m, 2.5 m and 6.5 degrees, respectively. Time series from the decay tests in surge, heave and pitch are shown in Figs. 6 – 8. Estimated natural periods are tabulated in Tab. 4. The natural periods are estimated over one cycle only, starting after one full cycle (to avoid any initial disturbances).

Figure 6a shows the grid dependence of the surge decay simulations. Due to the relatively long natural periods in surge motion, only two-three cycles has been simulated. Although that the grid refinement procedure is not perfectly systematic, a converging trend can be observed as the grid resolution is increased. However, grid convergence (a grid independent solution) has not been fully achieved and there are still small differences between the results with the two finest grid resolutions. Compared to experimental measurements, the numerical simulations over predicts the natural periods. The difference is only about 3.6% for the finest grid resolution, which can

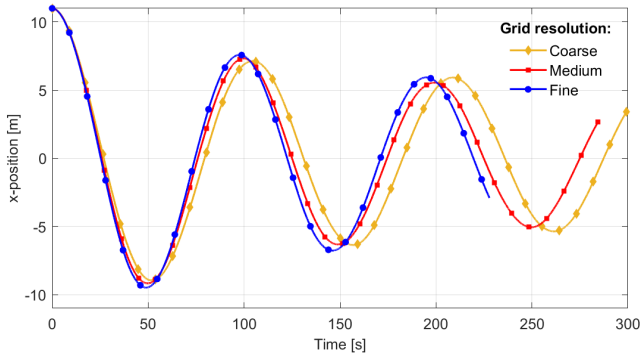

(a) Grid convergence study for surge decay.

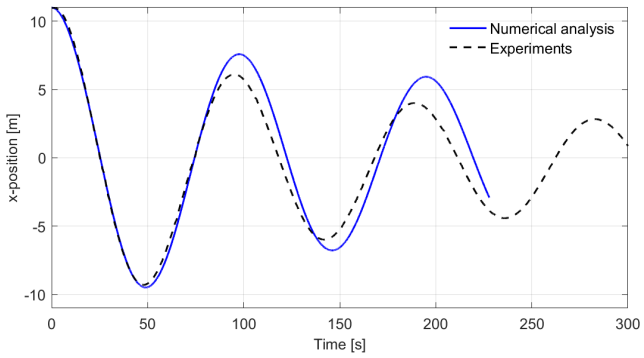

(b) Comparison between numerical results and experimental measurements.

Figure 6: Surge decay results.

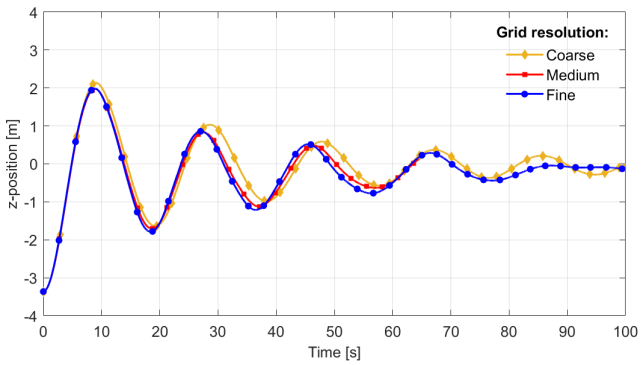

(a) Grid convergence study for heave decay.

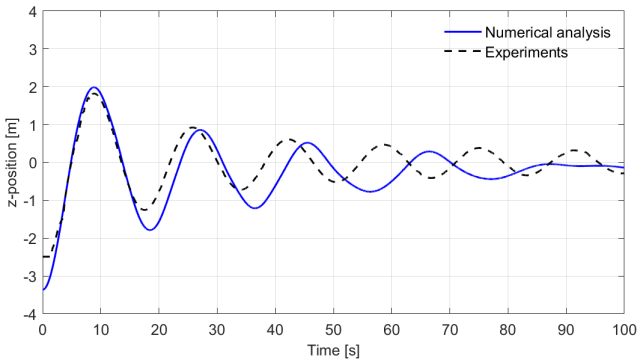

(b) Comparison between numerical results and experimental measurements.

Figure 7: Heave decay results.

be considered to be acceptable. One possible explanations for the discrepancy can be the way that the solid boundaries are implemented in the analysis. Using a forcing term (see Eq. (9)) approach smears out the boundary over a few grid cells, which may affect the accuracy of the platforms effective volume and added mass, thus altering the natural period. This is also evident from the numerical results' sensitivity to the grid resolution. There are also uncertainties in the experiments, but the uncertainty of the structural mass is expected to be less than 1%, which will give a negligible effect on the natural period (and is also a grid independent parameter). It is also expected that modelling of the mooring system is fairly accurate due to the linear stiffness property. It can also be observed in Fig. 6b that the damping is slightly less for the numerical simulations compared to the experimental measurements. Some deviations is reasonable to expect since the boundary layer is not fully resolved in the numerical analysis.

The heave decay results are shown in Fig. 7. Note that the results are slightly shifted such that the platform oscillates about a static equilibrium (mean position) at $z = 0$ m. The results are apparently converging as the grid resolution is increased, but convergence is not fully achieved. The difference between simulated natural period and measurement is about 8.4% for the finest grid. As for surge decay, it is anticipated that the discrepancy can be mainly explained by the treatment of the solid boundary in the numerical analysis. Treating the solid boundary as a diffuse boundary over a band of grid cells may alter the effective volume which affects the effective added mass and hydrostatic stiffness (buoyancy force). The horizontal mooring system has nearly no influence on the heave natural period, which is mainly governed by mass and added mass properties and the hydrostatic stiffness. The damping level is also slightly under predicted compared to the experiments.

The pitch decay results are presented in Fig. 8. The pitch motion appears to be less sensitive to the grid resolution compared to the surge and heave decay simulations. The variations in natural period is less than 1.7% between the finest and coarsest grid. The difference starts to become more noticeable first after 4-5 oscillations. Compared to the experimental measurements, the natural periods are slightly under predicted where the difference is about 2% for the finest grid (less for the coarser grids). There is also a small uncertainty in the measured vertical location of COG from the experiments, which may affect the actual moments of inertia and hydrostatic stiffness in pitch, and may explain why the simulated natural period converge towards a shorter period than the measured one. The damping is also slightly under predicted compared to experimental measurements, but in overall the simulated pitch decay compares well with the measurements.

4.2 *Regular waves*

Simulations of the platform in waves are carried out for two regular waves. Table 5 summarise the wave specifications used for the two test cases. In order to reproduce similar motion response of the platform, the numerical waves were first calibrated to match

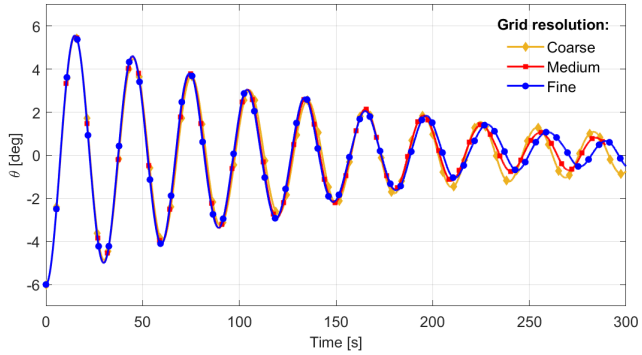

(a) Grid convergence study for pitch decay.

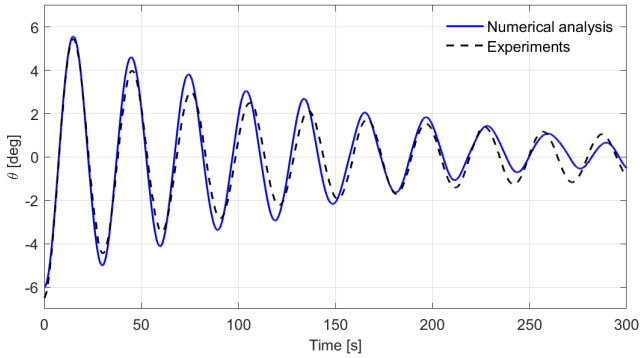

(b) Comparison between numerical results and experimental measurements.

Figure 8: Pitch decay results.

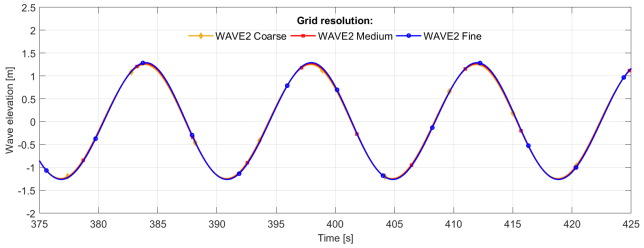

(a) WAVE2 grid convergence study.

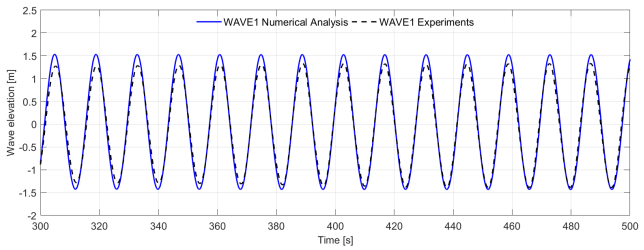

(b) WAVE1

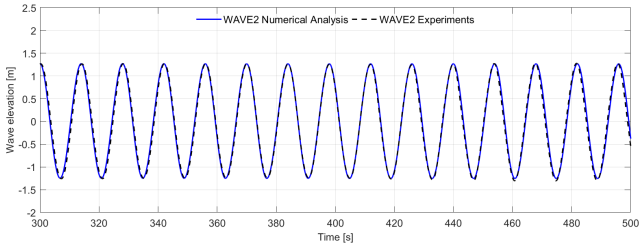

(c) WAVE2.

Figure 9: Wave elevation for test 2030.

Table 5: Wave height and period for regular wave tests.

	Wave	
Test no.	Height [m]	Period [s]
2030	2.55	14.0
2050	6.30	11.0

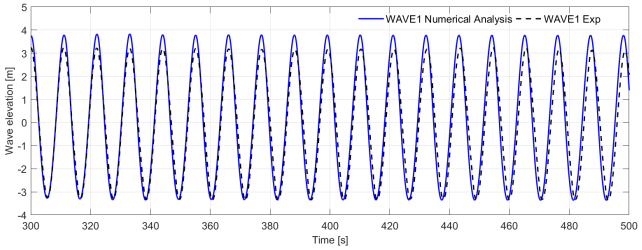

(a) WAVE1.

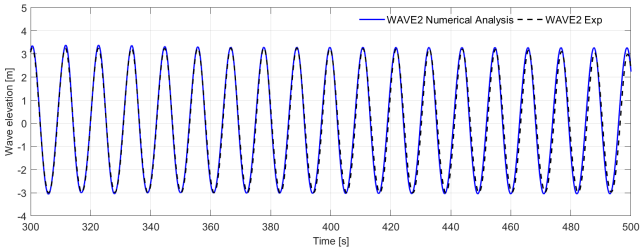

(b) WAVE2.

Figure 10: Wave elevation for test 2050.

the experimental waves. This was done using a two-dimensional representation of the numerical wave tank for more efficient calibration. The target was to match the numerical wave with the measured wave at the WAVE2-wave gauge (same location as the platform). Figures 9 and 10 show the results for tests 2030 and 2050, respectively. The wave gauge WAVE1 is located close to the wave generation zone and due to numerical dispersion of the wave it was necessary to generate a larger wave at the inlet in order to match the correct wave amplitude at WAVE2, thus the numerical wave at WAVE1 is somewhat larger than the measured wave. However, the numerical wave elevation at WAVE2 match the measured wave elevation very well for both test cases 2030 and 2050.

A grid convergence study of the wave was also carried out for test 2030. Only marginal differences can be seen between the different grid resolutions in Fig. 9a. The medium size grid resolution is therefore used in the three dimensional analysis. It is not expected that the selected resolution will provide a grid independent solution (based on the convergence study for the decay tests), but due to the need for a longer time duration of the simulation as well as a larger computational domain this was assumed to a be a practical trade-off to achieve an acceptable computational efficiency.

On the motion responses, Figs. 11 and 12 show the surge, heave and pitch motion of the platform for tests 2030 and 2050, respectively. As for test 2030, the wave induced surge response amplitude is slightly over estimated compared to the experimental mea-

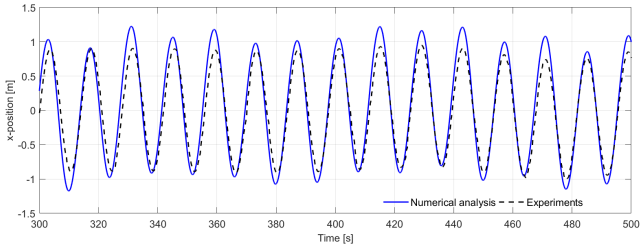

(a) Surge response.

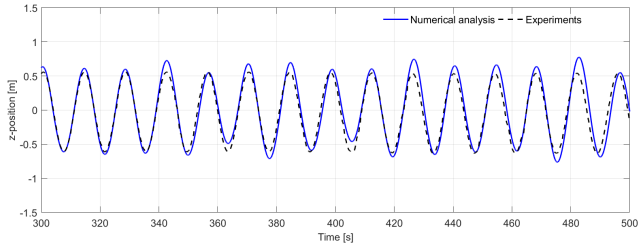

(b) Heave response.

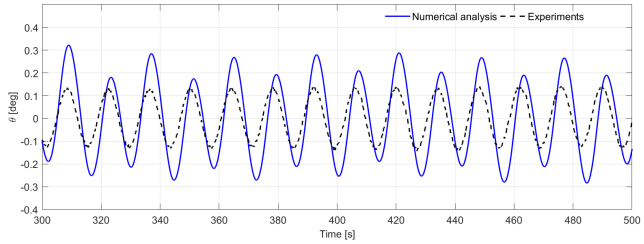

(c) Pitch response.

Figure 11: Motion responses for test 2030.

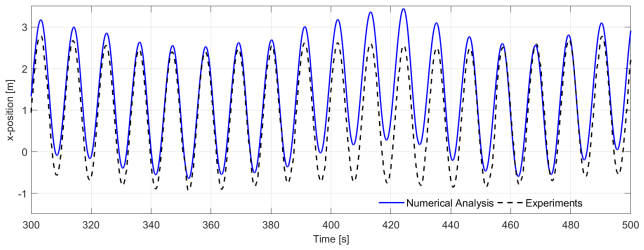

(a) Surge response.

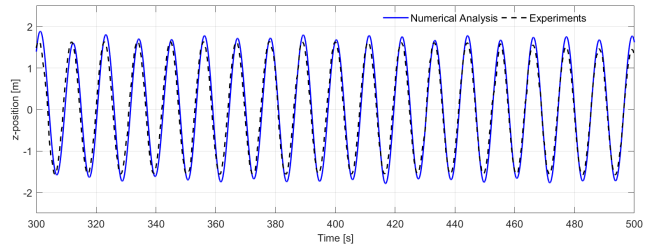

(b) Heave response.

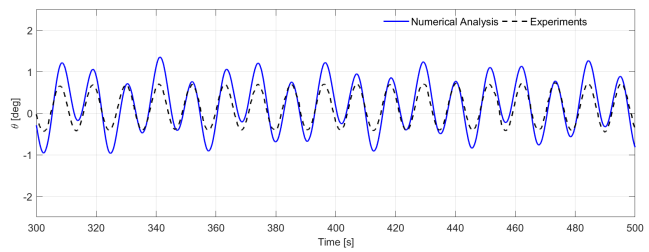

(c) Pitch response.

Figure 12: Motion responses for test 2050.

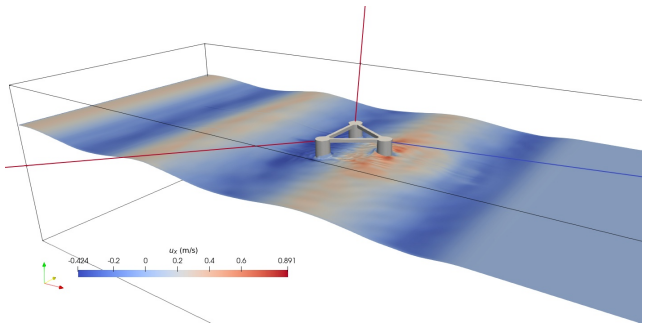

Figure 13: Screenshot of simulated wave-floater interaction for test 2050 showing horizontal velocity magnitude contours.

surements (see Fig. 11a), while for test 2050 (see Fig. 12a) the estimated amplitude is slightly less than the experiments. The simulated surge motion in test 2050 appears to be more offset than the experimental data. A low frequency variation in the surge motion can be observed in the experimental data, and the numerical calculations capture this slow variation well although the simulations appears to be a bit more pronounced than the experiments.

The calculated wave induced heave motions presented in Figs. 11b and 12b are in good agreement with the measurements. The calculated response show a small irregularity compared to the experimental data for test 2030. The pitch responses, as shown in Figs. 11c and 12c, are over estimated by the numerical simulations compared to the measurements. It should be pointed out that the pitch response amplitudes in the experiments are very small (about 0.1° in test 2030 and about 0.5° in test 2050) and values of relatively small magnitudes are generally difficult to calculate accurately.

The numerical wave tank with free surface elevation and velocity contours for test 2050 is shown in Fig. 13. The colours of the mooring lines denote the calculated tension in the lines. The colour of the free surface elevation corresponds to the horizontal velocity (u_x) in the numerical wave tank.

5 CONCLUDING REMARKS

The present paper presents numerical calculations of motion responses of a floating wind turbine substructure, the INO WINDMOOR semisubmersible FWT. The numerical simulations applies the level set method for modelling the free surface and a direct forcing method is used to calculate the hydrodynamic coupling between the fluid and the rigid body (6DOF) motion response. A linear spring system is applied to represent the mooring. Simulations of decay tests in surge, heave and pitch as well as simulations of the moored platform exposed to regular waves are carried out. Numerical results are compared with experimental data for validation of the results, and they show acceptable agreement with the measurements and the following observations are made:

- Surge and heave decay tests are more sensitive to the grid size than the pitch motion for the range of grid resolutions applied in the current analysis. The differences between the coarsest and finest grid are 7.3% and 6.1% for surge and heave natural periods, respectively, while it is only 1.7% for pitch. Calculated heave natural period has the largest deviations from the measurements, and the difference is about 8.4%. In particular, the heave natural period depends highly on how accurately the model calculates the hydrostatic stiffness (buoyancy force) and added mass force - which is believed to be very sensitive to the grid resolution.
- The numerically generated waves need to be calibrated to the measured waves in order to ensure similitude of the wave loads on the floating platform. In the present results, it is shown that the wave elevation and propagation is not noticeably sensitive to the grid resolution applied in the analysis.
- Comparison to measured data shows that wave induced surge and heave responses are calculated well, with only small deviations. The calculated wave induced pitch responses are more significantly over estimated compared to the measurements, but the measured pitch responses are very small and responses of relatively small magnitudes are generally difficult to predict accurately.

ACKNOWLEDGEMENTS

The authors are grateful for the grants provided by the Research Council of Norway under the HAVBRUK2 programme (grant no. 267981). The authors are also grateful to the WINDMOOR project, funded by the Research Council of Norway under the ENERGIX programme (grant no. 294573) for access to experimental data of the INO WINDMOOR floating substructure. The computations were performed on resources provided by UNINETT Sigma2 - the National Infrastructure for High Performance Computing and Data Storage in Norway (project no. NN2620K)

REFERENCES

Ashby, S. F. & R. D. Falgout (1996). A parallel multigrid preconditioned conjugate gradient algorithm for groundwater flow simulations. *Nuclear Science and Engineering 124*(1), 145–159.

Bihs, H. & A. Kamath (2017). A combined level set/ghost cell immersed boundary representation for floating body simulations. *International Journal for Numerical Methods in Fluids 83*(12), 905–916.

Bihs, H., A. Kamath, M. A. Chella, A. Aggarwal, & Ø. A. Arntsen (2016). A new level set numerical wave tank with improved density interpolation for complex wave hydrodynamics. *Computers & Fluids 140*, 191–208.

Carrica, P. M., R. V. Wilson, R. W. Noack, & F. Stern (2007). Ship motions using single-phase level set with dynamic overset grids. *Computers and fluids 36*(9), 1415–1433.

Fadlun, E., R. Verzicco, P. Orlandi, & J. Mohd-Yusof (2000). Combined immersed-boundary finite-difference methods for three-dimensional complex flow simulations. *Journal of computational physics 161*(1), 35–60.

Hirt, C. & B. Nichols (1981). Volume of fluid (vof) method for the dynamics of free boundaries. *Journal of Computational Physics 39*, 201–225.

Jacobsen, N. G., D. R. Fuhrman, & J. Fredsøe (2012). A wave generation toolbox for the open-source CFD library: OpenFoam. *Int J Numer Methods Fluids 70*(9), 1073–1088.

Jiang, G.-S. & D. Peng (2000). Weighted ENO schemes for Hamilton-Jacobi equations. *SIAM J. on Scientific Computing 21*, 2126–2143.

Jiang, G.-S. & C.-W. Shu (1996). Efficient impementation of weighted ENO schemes. *J. Comput. Phys. 126*(1), 202–228.

Martin, T., A. Kamath, & H. Bihs (2021). Accurate modeling of the interaction of constrained floating structures and complex free surfaces using a new quasistatic mooring model. *International Journal for Numerical Methods in Fluids 93*(2), 504–526.

Martin, T., A. Tsarau, & H. Bihs (2021). A numerical framework for modelling the dynamics of open ocean aquaculture structures in viscous fluids. *Applied Ocean Research 106*.

Mayer, S., A. Garapon, & L. S. S. Ørensen (1998). A fractional step method for unsteady free-surface flow with applications to non-linear wave dynamcis. *Int. J. Numer Methods Fluids 28*, 293–315.

Osher, S. & J. A. Sethian (1988). Fronts propagating with curvature-dependent speed: algorithms based on Hamilton-Jacobi formulation. *J. Comput Phys. 79*, 12–49.

Ramaswamy, B., M. Kawahara, & T. Nakayama (1986). Lagrangian finite element method for the analysis of two-dimensional sloshing problems. *International Journal for Numerical Methods in Fluids 6*(9), 659–670.

Sauder, T., V. Chabaud, M. Thys, E. E. Bachynski, & L. O. Sæther (2016). Real-time hybrid model testing of a braceless semi-submersible wind turbine: Part i—the hybrid approach. In *International Conference on Offshore Mechanics and Arctic Engineering*, Volume 49972, pp. V006T09A039. American Society of Mechanical Engineers.

Souza, C., P. A. Berthelsen, L. V. Eliassen, E. E. Bachynski, E. Engebretsen, & H. Haslum (2021). Definition of the INO WINDMOOR 12 MW base case floating wind turbine. Tech. Rep. OC2020 A-044, SINTEF Ocean.

Sussman, M., P. Smereka, & S. Osher (1994). A level set approach for computing solutions to incompressible two-phase flow. *J. Comput Phys. 114*, 14–159.

Thys, M., C. Souza, T. Sauder, N. Fonseca, P. A. Berthelsen, E. Engebretsen, & H. Haslum (2021). Experimental investigation of the coupling between aero-and hydrodynamical loads on a 12 mw semi-submersible floating wind turbine. In *International Conference on Offshore Mechanics and Arctic Engineering*, Volume 85192, pp. V009T09A030. American Society of Mechanical Engineers.

Timmermans, L., P. Minev, & F. Van De Vosse (1996). An approximate projection scheme for incompressible flow using spectral elements. *Int. J. for Numerical Methods in Fluid 22*, 673–688.

Uhlmann, M. (2005). An immersed boundary method with direct forcing for the simulation of particulate flows. *Journal of computational physics 209*(2), 448–476.

van der Vorst, H. (1992). BiCGStab: A fast and smoothly converging variant of Bi-CG for the solution of nonsymmetric linear systems. *SIAM J. on Scientific and Statistical Computing 13*, 631–644.

Yang, L. (2018). One-fluid formulation for fluid-structure interaction with free surface. *Computer Methods in Applied Mechanics and Engineering 338*, 102–135.